



One-shot additive manufacturing of robotic finger with embedded sensing and actuation

Gianni Stano^{1,2} · S M Al Islam Ovy² · Jakob Ryan Edwards² · Matteo Cianchetti^{3,4} · Gianluca Percoco¹ · Yonas Tadesse²

Received: 15 July 2022 / Accepted: 16 November 2022 / Published online: 23 November 2022
© The Author(s) 2022

Abstract

A main challenge in the additive manufacturing (AM) field is the possibility to create structures with embedded actuators and sensors: addressing this requirement would lead to a reduction of manual assembly tasks and product cost, pushing AM technologies into a new dimension for the fabrication of assembly-free smart objects. The main novelty of the present paper is the one shot fabrication of a 3D printed soft finger with an embedded shape memory alloy (SMA) actuator and two different 3D printed sensors (strain gauge and capacitive force sensor). 3D printed structures, fabricated with the proposed approach, can be immediately activated after their removal from the build plate, providing real-time feedback because of the embedded sensing units. Three different materials from two nozzles were extruded to fabricate the passive elements and sensing units of the proposed bioinspired robotic finger and a custom-made Cartesian pick and place robot (CPPR) was employed to integrate the SMA spring actuator into the 3D printed robotic finger during the fabrication processes. Another novelty of the present paper is the direct integration of SMA actuators during the 3D printing process. The low melting thermoplastic polycaprolactone (PCL) was extruded: its printing temperature of 70 °C is lower than the SMA austenitic start temperature, preventing the SMA activation during the manufacturing process. Two different sensors based on the piezoresistive principle and capacitive principle were studied, 3D printed and characterized, showing respectively a sensitivity ratio of change in resistance to finger bending angle to be $674.8 \frac{\Omega}{^\circ \text{Angle}}$ and a capacitance to force ratio of $0.53 \frac{\text{pF}}{\text{N}}$. The proposed manufacturing approach paves the way for significant advancement of AM technologies in the field of smart structures with embedded actuators to provide real-time feedback, offering several advantages, especially in the soft robotics domain.

Highlights

- One shot fabrication of a smart bioinspired finger equipped with a shape memory alloy (SMA) actuator, piezoresistive strain gauge and capacitive sensor
- Automated integration of the SMA spring actuator during the 3D printing process by exploiting the low melting thermoplastic polycaprolactone and a pick and place robot
- Study of the process parameters to reduce the 3D printed strain gauge resistance of 142%

Keywords 3D printed functional structure · Embedded sensors and actuators · Robotic finger · Intelligent structure · Soft robotics

✉ Gianluca Percoco
gianluca.percoco@poliba.it

- ¹ Department of Mechanics, Mathematics and Management, Polytechnic University of Bari, Via E. Orabona 4, 70125 Bari, Italy
- ² Humanoid, Biorobotics and Smart Systems (HBS) Laboratory, Department of Mechanical Engineering, The University of Texas at Dallas, Richardson, TX 75080, USA
- ³ The BioRobotics Institute, Scuola Superiore Sant'Anna, 56025 Pisa, Italy
- ⁴ Department of Excellence in Robotics & AI, Scuola Superiore Sant'Anna, 56025 Pisa, Italy

1 Introduction

Recently, Additive Manufacturing (AM) technologies have started gaining a lot of interest in the soft robotics and bio-medical field [1], due to several intrinsic features such as the possibility to: (i) employ soft materials, (ii) easily create complex structures, (iii) use more materials in the same manufacturing cycle, and (iv) fabricate smart structures [2–6]. Among the different material extrusion techniques, Fused Filament Fabrication (FFF) technology, seems to fit well with soft robotics requirements: in particular, as pointed

out by Shintake et al. [7], several researchers focused on the study (design, optimization, simulation, fabrication, and control) of soft grippers. It is possible to classify the contribution of FFF into the soft robotic field as a function of the actuation mechanism underlying the fabricated soft robot, as follows: pneumatic actuation, shape memory polymers and tendon driven. 3D printed pneumatic actuators consist of a main body made up of soft material actuated by means of compressed air. The main body can be patterned in different ways to achieve several kinds of deformations (such as bending, twisting, elongating, and shortening). The bending actuator is the most widespread class fabricated by means of FFF [8]. Some examples of bending pneumatic actuators equipped with strain sensors (fabricated using a dual extruder machine) are provided in [9–11]. Several results have been achieved in this field such as: (i) a way to improve the object grasping capability, (ii) the possibility to fabricate embedded air connectors [12] and (iii) the possibility to obtain helicoidal motion [13]. Shape memory polymers actuator is based on phase change of the materials such that the change of Young's modulus when the switching temperature (T_s) is reached resulting in a change of material softness. FFF has been largely employed for the fabrication of structures based on this actuation method [14–17] proving how printing parameters (infill and pattern) affect recovery time and recovery quality [18]. A new and promising way to exploit the shape memory effect in FFF structures is the creation of structures made up of at least two parts: joints made of shape memory polymers and links made of non-shape memory material. This design choice implies several advantages: (i) the time required to activate only the joint is just a couple of seconds (compared to more than 30 s to activate the whole structure), (ii) it is possible to take full advantage of multi-material 3D printing, and (iii) complex movements are enabled [19–23]. Finally, tendon-driven-based FFF robots have been largely exploited over the past few years and it consists of creating structures (for example fingers) actuated utilizing cables connected to motors. In [24] a soft manipulator has been fabricated using a custom-made FFF machine enabling the bonding strength when different materials (hard and soft) are extruded. The authors studied the best hinge geometry providing a new finger version (reducing the phalanges dimension) to improve the finger conformability around unknown objects for grasping tasks. Mohammadi et al. demonstrated that this approach can be used to fabricate a fully 3D printed hand (34 h for the manufacturing) costing 200 USD and characterized by at least 1 year of lifetime which can be employed as prostheses [25].

Shape memory alloys (SMAs) are a very promising class of actuators, largely employed in soft robotics to actuate soft structures: they are smart materials able to change their crystalline structure from martensite to

austenite when thermally activated, leading to a change of young's modulus. Compared to the above-mentioned actuation methods, SMAs do not require heavy systems to work such as pneumatic compressors or motors and their actuation is faster and less power-consuming than shape memory polymers. Silicone molding is the most used fabrication technique to embed SMAs into elastomeric matrices to achieve several kinds of motion such as bending and twisting [26–29].

Recently, AM has been used to fabricate structures activated by SMA, showing at the same time: (i) all the potentialities of AM technology (capability to create complex structures, capability to obtain complex motion paths using two materials with different stiffness in the same printing cycle), and (ii) a huge problem related to the manual embedding of SMAs wires after the fabrication [30, 31]

The accurate placement of SMAs into 3D printed structures is a big challenge and addressing this requirement would abruptly increase the impact of FFF in soft robots manufacturing, as a matter of fact solving this problem would (i) reduce the manual tasks leading to a completely automated manufacturing process, (ii) increase the accuracy of the SMAs placement and (iii) allow the placement of SMAs into complex structures. Although several interesting solutions have been discovered in the field of FFF fiber reinforcement [32–34] and wires placement [35], they cannot be applied to SMAs integration due to the high extrusion temperature of the common FFF filaments (180 to 250 °C), far above the austenitic start temperature threshold of SMAs.

The main goal of the proposed research is the one shot additive manufacturing of a soft robotic finger with embedded sensors (capacitive and resistive) and actuator (SMA spring) without recurring to assembly task. In this way, the 3D printed part results ready to be activated, providing feedbacks thanks to the sensor, after the removal from the machine build plate. At the best of the authors' knowledge, despite a huge exploitation of FFF for the fabrication of 3D printed sensors [36–42] and actuators, structures equipped with both sensors and actuators have not been manufactured yet.

A flexible manufacturing approach to solve the problem of the automated SMAs placement into FFF structures is presented: using a commercial and inexpensive (300 USD) dual extruder FFF machine and a pick and place robot. The key enabler of the present research is related to the use of a material characterized by a printing temperature (T_p) lower than the SMA austenitic starting temperature (A_s): polycaprolactone (PCL) filament (extruded temperature of 70° C) in conjunction with a SMA spring, having A_s equal to 90° C has been employed.

The present research aims to show that, using the proposed manufacturing approach, it is possible to create

smart active structures closing the loop between actuation and sensing without recurring to any post-processing and assembly task.

2 Materials and methods

The main goal of the present work is the one-shot additive manufacturing of a soft robotic finger equipped with 3D printed sensing systems (a strain gauge for the bending sensing and a capacitive force sensor for the object detection) and a SMA spring actuator (see Fig. 1). To achieve this goal, a low-cost multimaterial extrusion machine and a custom-made Cartesian pick and place robot (to automatically embed the SMA spring) were employed. The proposed manufacturing approach aims to push the role of AM into a new dimension: structures having the capability to provide real-time feedbacks and with embedded actuation systems can be fabricated in a fully automated way without recurring to assembly tasks.

2.1 Compatibility among extruded material and SMA

Apparently, a huge temperature incompatibility issue occurs when SMAs need to be embedded, during the fabrication process, into FFF parts: generally, flexible materials such as common thermoplastic polyurethanes (TPUs) are characterized by a printing temperature (T_p) of 220 °C, far above the A_s of Nickel-Titanium SMAs (ranging from 70 to 90 °C). The aim of automating the SMA placement into 3D printed parts motivated the authors to pause and restart the printing process in order to embed the SMA using a pick and place robot. This task has been made possible by exploiting polycaprolactone (PCL) filament: a non-conventional material, mainly used in the biomedical field for scaffold manufacturing [43–46]. PCL material is characterized by a T_p ranging from 70 to 110 °C: it results compatible with SMAs' A_s without affecting its thermal memory. PCL is also well-known for getting softer when locally heated up to a temperature close to T_p . This behavior will take place when the SMA will be activated through the Joule effect. PCL (eMate-PCL, eSun, China) was used in this study, while

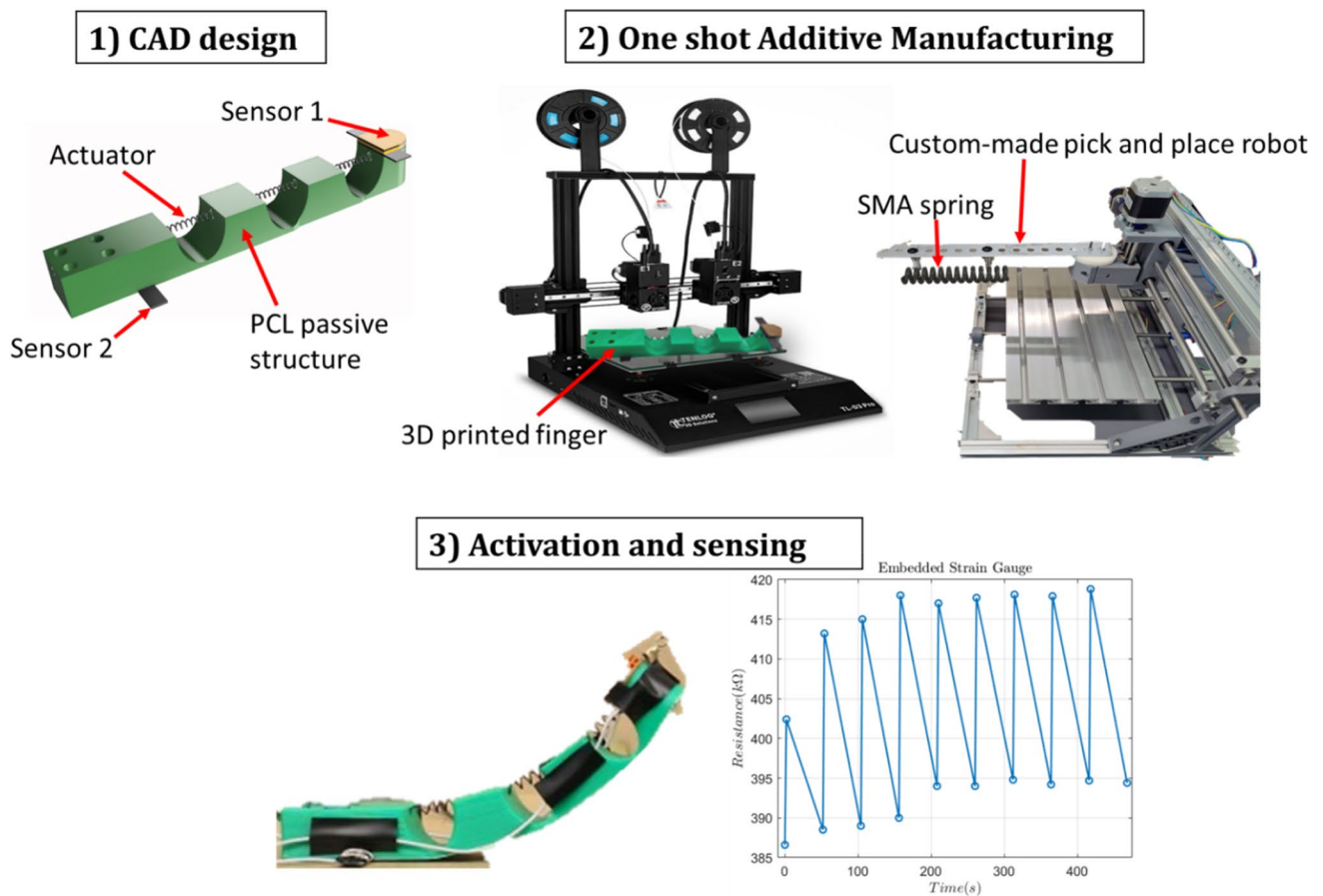


Fig. 1 Research workflow

a Dynalloy Inc. SMA spring with A_s equal to 90 °C was employed (discussed in Section 2.2). PCL process parameters and softness behavior are analyzed in the “PCL process parameters” Sections 2.1.1 and 2.1.2, respectively.

2.1.1 PCL process parameters

The main process parameters to take into account through the present work are (i) printing temperature (T_p), (ii) printing speed (s), nozzle size (d) and layer height (h). In regard to T_p , the authors decided to set the minimum temperature in the range suggested by the filament manufacturer [70, 110] °C, to avoid any interaction to A_s (equal to 90 °C) during the SMA integration. As well-known from scientific literature [47], s mainly affects the printing quality (dimensional accuracy and surface roughness): with a trial and error approach, we found 15 mm/s and 10 mm/s around the corners to be the best s values to set ensuring a good printing quality.

PCL material is stiffer than classic TPU (used for the fabrication of soft robots such as fingers) but softer than PLA: in Table S1 (Supplementary information) a comparison among the main mechanical properties of these 3 filaments is provided. The PCL structure should be easily deformable by the SMA actuators: a study on the stiffness has been conducted. To address this requirement, the relationship among d , h and weight of PCL structures was studied using a factorial plan 2^2 . The factorial plan is described in Supplementary information, section S2.

From the plan, several considerations can be drawn:

- The two factors (namely d and h , see Supplementary information, S2) affect the weight (g) of the structure while the interaction among the two factors does not affect the weight (see Fig. S1).
- The way in which the two main parameters affect the weight of the PCL structures (shown in Fig. S1) is:
 - i) nozzle size: switching from a 0.4 mm to a 1 mm nozzle size, the weight increases.
 - ii) layer height: switching from 0.2 mm to 0.4 mm, the weight increases.
- The residual analysis shows the consistency and robustness of the computed factorial plan (see Fig. S1).

In summary, the 2^2 factorial plan provides the best d and h value to set, to create a lightweight structure which is found to be 0.4 mm, and 0.2 mm respectively. The four most important process parameters for the proposed application have been analyzed and listed in Table 1.

2.1.2 PCL compliance

In this section, the relationship between PCL compliance and local heating is studied. Several PCL samples with embedded resistive wire (Nichrome wire, diameter 0.5 mm) have been fabricated. The sample dimensions were 70, 35, and 10 mm in size along the x, y, and z-axis. The printing process was stopped to embed the resistive wire and later resumed to incorporate the resistive wire into the PCL structure (see Fig. 2). The resistive wire has the function to mimic the SMA actuator: it was heated up in the same range of SMA temperature (up to 110 °C) which will be used for actuation later.

The compliance of a structure is calculated as follows:

$$Cm = \frac{1}{S} \quad (1)$$

where Cm [mm/N] is the compliance and S is the stiffness, calculated as follows-

$$S = \frac{F}{d} \quad (2)$$

where F is the applied force [N] and d is the sample displacement [mm].

An ad hoc set-up was used to evaluate the change of compliance, it consists of (i) a power supply to heat up the embedded resistance, (ii) a thermal imaging camera to evaluate the actual temperature of the wire, (iii) a calibrated weight (2.5 N) connected to the sample (see Fig. 2a), and (iv) a digital camera to take pictures at each increment of temperature to calculate the displacement. The applied force was the same for each temperature increment and the only variable to measure was the displacement of the tip (see Fig. 2b): in this way the compliance variation was measured.

Starting from T_{room} , the temperature of the embedded resistive wire was incrementally increased, and a picture was taken from 70 °C up to 110 °C with a step of 10 °C. Three PCL samples were analyzed, with three tests done for

Table 1 Summary of process parameters for PCL and SMA

Parameter	Value	Expected advantage
Printing temperature (T_p)	70 °C	Avoid affecting SMA programming
Printing speed (s)	15 and 10 (near the corner) mm/s	Increase printing quality
Nozzle size (d)	0.4 mm	Reduction of weight
Layer height (h)	0.2 mm	Reduction of weight

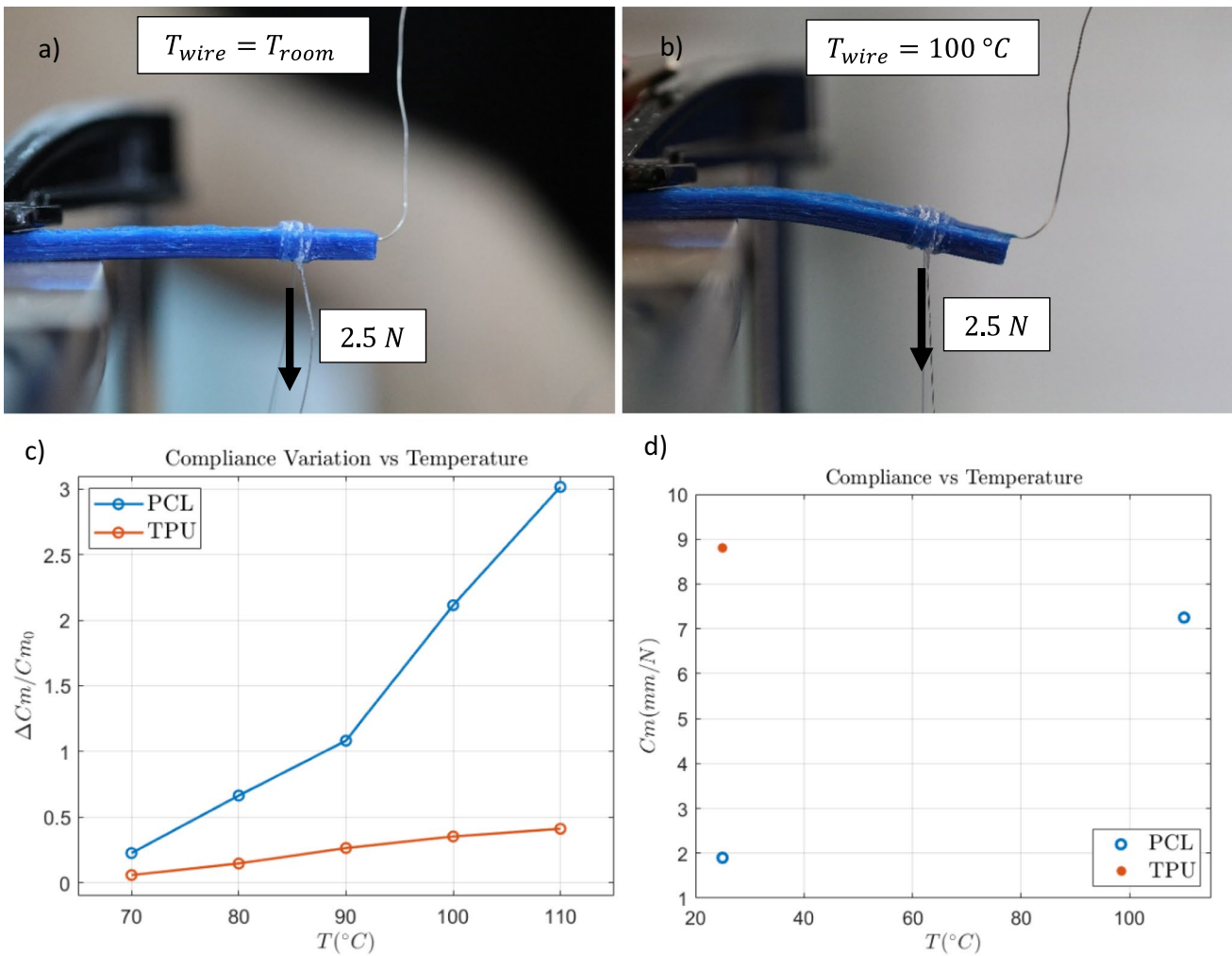


Fig. 2 (a) Tested sample when $T_{wire} = T_{room}$, and (b) $T_{wire} = 100\text{ }^{\circ}\text{C}$. (c) $\Delta C_m / C_{m0}$ vs T for PCL and TPU, (d) absolute compliance vs T for PCL and TPU: only one point for TPU is shown in order to dem-

onstrate that the PCL compliance at $110\text{ }^{\circ}\text{C}$ is close to the TPU compliance at room temperature

each sample, resulting in a statistically insignificant standard deviation (see Table 2).

A significant change in compliance ΔC_m compared to the initial compliance C_{m0} of almost 6 times occurs when the resistive wire is heated up to $110\text{ }^{\circ}\text{C}$ (the maximum temperature that will be reached from the embedded SMA) making this material suitable for the proposed application (see Fig. 2c). To have a direct comparison with TPU, the same identical tests were performed on TPU showing a maximum change in compliance $\Delta C_m / C_{m0}$ of 0.4 (86% less than PCL): these data refer to the mean among 3 samples for PCL and TPU. From these tests, it is possible to get a comparison in terms of absolute compliance: when PCL is locally heated up to $110\text{ }^{\circ}\text{C}$ (same temperature that will be reached by the SMA), its absolute compliance is almost 7 mm/N not that far from the compliance of TPU at T_{room} (almost 9 mm/N). See Fig. 2d).

In conclusion, PCL material appears to be the right candidate to match with SMA integration, not only because of its low printing temperature but also because its compliance abruptly increases when it is locally heated up, making PCL soft when SMA will be heated to be actuated.

2.2 SMA actuators

For the current study, a shape memory alloy (SMA) spring with the following properties was used: (i) T_{as} equal to $90\text{ }^{\circ}\text{C}$, (ii) internal diameter equal to 0.51 mm , and (iii) external diameter of 3.45 mm (see Fig. S2). It is important to note that the printing temperature of PCL equal to $70\text{ }^{\circ}\text{C}$ helped the integration of the SMAs, otherwise, it would have been impossible to integrate SMA with lower A_s without adversely affecting its thermomechanical behavior.

Table 2 PCL samples: change in compliance $\Delta C_m/C_0$ vs temperature

T [°C]	Sample1 $\Delta C_m/C_m0$ [mm/N]		Sample2 $\Delta C_m/C_m0$ [mm/N]		Sample3 $\Delta C_m/C_m0$ [mm/N]	
	mean	Std.dev	mean	Std.dev	mean	Std.dev
70	0.229	<0.001	0.209	<0.001	0.241	<0.001
80	0.659	<0.001	0.665	<0.001	0.672	<0.001
90	1.09	0.02	0.98	0.01	1.18	0.03
100	2.05	0.04	2.12	0.03	2.17	0.06
110	2.99	0.11	3.08	0.16	2.97	0.14

The length of the SMA spring depends on the finger dimensions (see Section 3.1), being the finger length equal to 122 mm, an overall spring length (in its extended state, including the two terminal-crimps as well) bigger than that threshold value is required.

The length of the only SMA spring in its extended state (in its pretension state) was 92 mm: 20 mm shorter than the finger length, in fact after crimping it with terminal metal crimps, it reached 140 mm in length.

Before embedding the SMA into the 3D printed structure, it has been characterized using a custom-made setup following [48, 49] (See supplementary information section S3, and Fig. S3) to determine the relationships between input and output. The following time-domain properties: applied current, voltage, displacement, temperature, and force were obtained. Three different current inputs were provided (2.8 A, 3.2 A and 3.6 A) for 2 s, followed by an off period of 50 s (corresponding to a frequency of 0.02 Hz): for each current input the following protocol was applied for a total of 5 cycles. The characterization results are summarized in Fig. 3a and b. From the SMA characterization, it stands out that the best current value to apply is 3.2 A, for the following reasons:

- By applying 3.2A input current, the SMA temperature values reached a temperature of 110 °C, it corresponds to the highest compliance in PCL material (Section 2.1.2). The other two current inputs, 2.8 A and 3.6 A, provide respectively inadequate temperature to take full advantage of the PCL behavior and a too high-temperature value (around 160 °C) which would melt the PCL finger.
- The average displacement obtained providing 3.2A is 11.2 mm, while the one obtained at 3.6 A is 11.5 mm: these two values are very close but using 3.2 A it is possible to reduce the power consumption.
- The same observation can be seen with the force values: almost identical force values are reached providing 3.2 A and 3.6 A. Also, in this case, providing 3.2 A, the power consumption is reduced.

3 Design and sensor evaluation

3.1 Soft finger design

To prove the potentialities of the proposed manufacturing approach, a soft finger with embedded sensors and a SMA spring actuator was fabricated in a single shot. We followed the design rules pointed out by Mutlu et al. [24] for this work.

The proposed finger (see Fig. 4a and b) can be subdivided into two portions: the active finger and a terminal block equipped with 4 holes to fix the finger to a custom-made platform during the tests. Finger dimensions are provided in S4 (Supplementary information). The hole in which the SMA spring will be embedded during the printing process is one of the most important parts of the finger. It has been drawn with the following features: (i) diameter of 4 mm (with a trial-and-error approach, this value was found to be the best diameter to ensure a complete and full embedding of the SMA spring) and (ii) above the neutral axis of the structure to provide a better bending when the SMA is activated.

The finger is equipped with two sensors which will be manufactured in the same printing cycle as the finger. In the bottom part of the finger, a strain gauge sensor has been drawn: it consists of 4 tracks having an active length of 84 mm and a width of 1.2 mm. A distance between two adjacent tracks of 1.2 mm was set. Also, end-loops (3.6 mm × 4 mm) were included to reduce stress sensitivity in the axis perpendicular to the deformation axis and to improve the measurement quality. The strain gauge geometry is shown in Fig. 4c.

The second sensor is placed on the tip of the finger, and it is used as a force/contact sensor. The sensor is based on the capacitive principle, and it has been fabricated using the same conductive material employed for the strain gauge and a different insulator material from PCL named NinjaFlex, well known for being one of the softest commercially available filaments. More details about the two just discussed sensors are provided in the next Section 3.2.

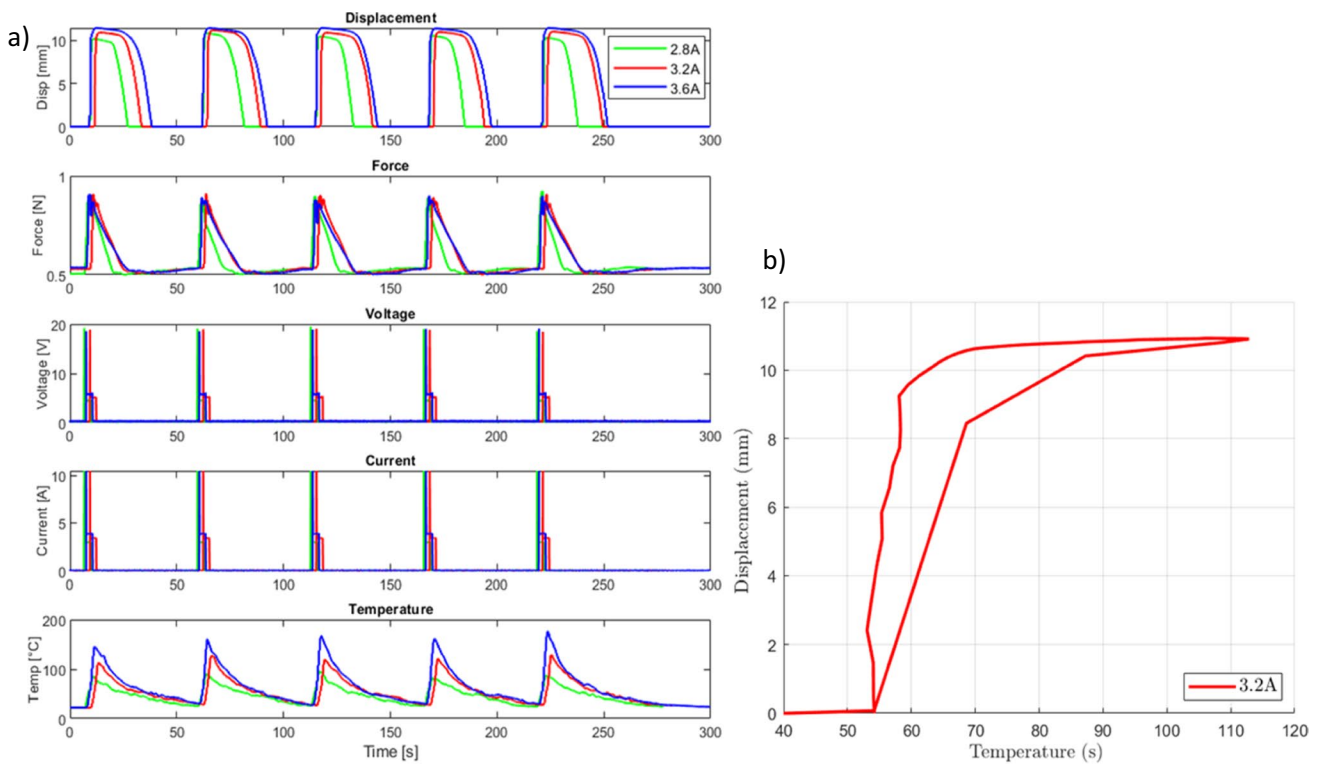


Fig. 3 SMA characterization of 0.51 mm wire diameter, 3.45 mm coiled diameter, 92 mm length spring: (a) overall results for five consecutive cycles at different current inputs, and (b) relationship tem-

perature-displacement for the first cycle (time 0 to 13 s corresponding to the peak of temperature) at 3.2A

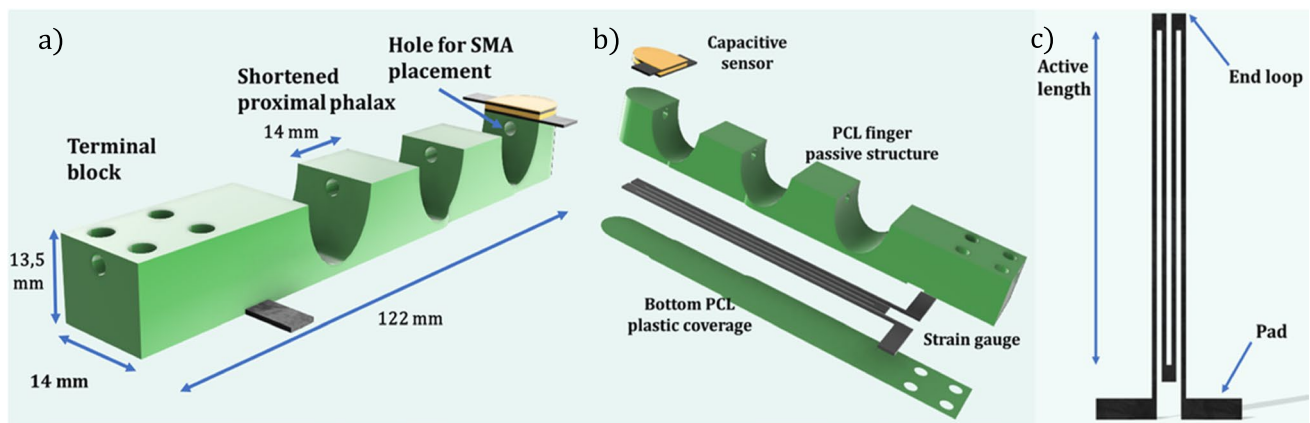


Fig. 4 Proposed finger: (a) finger dimensions, (b) finger components, and (c) strain gauge

3.2 Sensor evaluation

Here in this section, the two manufactured sensors are analyzed and studied, showing all the potentialities of the dual extruder FFF technology in the manufacturing of embedded sensors. It is important to point out that the two proposed sensors are based on two different working principles:

piezoresistive (change in electrical resistance) and capacitive (change in capacitance). In this work, we are showing for the first time, to the best of the authors’ knowledge, two sensors based on different principles are 3D printed and embedded in the same structure and evaluated in a fully functional robotic/ prosthetic finger.

3.2.1 Strain gauge

The dimensions of the proposed strain gauge sensor are described in Section 3.1. The length and the width are the same as the “active finger”. Exploiting the piezoresistivity effect (Eq. (3)), the strain gauge will provide a change in resistance when the finger will be actuated. The goal of embedding the strain gauge is to correlate the finger bending angle to the change of resistance and to have direct and real-time feedback.

$$R = \rho \frac{l}{A} \quad (3)$$

where $R(\Omega)$ is the strain gauge electrical resistance, $\rho(\frac{\Omega}{mm})$ is the material resistivity (a constant value which does not depend on the geometry), $l(mm)$ is the track length, and $A(mm^2)$ is the track surface area. When a stimulus is applied (i.e., bending, compression, tension and so on), only the $\frac{l}{A}$ ratio changes, leading to a change in the final strain gauge resistance R . FFF-based strain gauges [50] have been largely employed and several experimental and theoretical studies have been performed to improve the scientific knowledge in this field under different points of view (i.e., dynamic piezoresistivity [36], thermal effects [51, 52] and modelling of anisotropic electrical conductivity [53]).

The sensors were manufactured using a conductive thermoplastic polyurethane (CTPU), namely NinjaTek Eel, NinjaTek, USA, to address severe bending that would break conductive polylactic acid (henceforth CPLA). CTPU material data are provided in Section 3.2.2. One of the problems related to the fabrication of resistive sensors through FFF is the high electrical resistance (low conductivity) [54] involving electrical losses: as a matter of fact, these kinds of filament are made up of a polymeric matrix doped with conductive fillers (such as carbon black, carbon nanotubes and so on). To minimize the electrical resistance, it is important to study FFF process parameters to find out a correlation between them and the increase of conductivity. So far, in scientific literature, it has been proved that layer height and printing orientation affect the final electrical resistance in 3D printed strain gauges [55]. In the present paper, two more process parameters have been studied, correlating their effect to the final electrical resistance of the 3D printed samples: printing pattern P_p and printing temperature T_p .

Considering P_p , the only 3 different patterns allowed by the combination between active strain gauge width (1.2 mm) and employed nozzle size (0.4 mm) were studied, the three P_p analyzed are 3 lines (called “A”), line-zigzag-line (called “B”) and only zigzag (called “C”). The idea underlying the study of the best printing pattern is to investigate if it is possible to manufacture an optimal path for the current.

Considering T_p , 2 different values were changed, 230 °C (called “X”) and 240 °C (called “Y”): the minimum and the

maximum value suggest by the filament manufacturer. The idea, in this case, is to investigate if the temperature affects the final electrical resistance. The studied process parameters are listed in Table 3.

A manufactured plan based on a total of 3 repetitions for each combination (fabricated in a random order to reduce the impact of external factors) was followed, and two outputs were measured for each combination: i) mean final electrical resistance (using a benchtop multimeter) and ii) standard deviation. The 3D printed samples consist of a 0.4 mm substrate of TPU and the proposed strain gauge (same dimension as Section 3.1). In Fig. 5, the sample CAD model, the theoretical printing pattern generated by the slicing software (Ultimaker Cura 4.11) and the actual 3D printed tracks are shown.

The results of the parameter investigation are shown in Fig. 5c and d.

From the results, the following conclusions can be drawn:

- Both the studied process parameters, statistically affect the electrical resistance of the proposed strain gauge.
- For each printing pattern, the increase of the printing temperature from 230 °C up to 240 °C involves a huge decrease in the final electrical resistance respectively of 27.6%, 36.5% and 32.1% for A, B and C. Also, the standard deviation decreases respectively of 35.1%, 39.2% and 52.2% for A, B and C, when T_p switches from X (230 °C) to Y (240 °C). In the authors’ opinion, this behavior is related to the melting process of the conductive filler (carbon black) scattered into the TPU matrix: in accordance with the percolation theory, the conductivity of conductive polymers is due to the creation of conductive network in which the electrical current can flow. Because the size of carbon black nanoparticles scattered into the TPU matrix is not uniform (the melting point of conductive fillers depends on its size [56]), increasing the printing temperature (namely the melting point of the carbon-black), the probability that more carbon black is melted increases, and also the probability to create a stronger conductive network for the current flow increases too. For this reason, for each pattern when the printing temperature increases, the

Table 3 Process parameters studied for resistance minimization

Printing pattern (P_p)- Printing temperature (T_p)	Name
3 lines (P_p)	A
Line- zigzag- line (P_p)	B
Zigzag (P_p)	C
230 °C (T_p)	X
240 °C (T_p)	Y

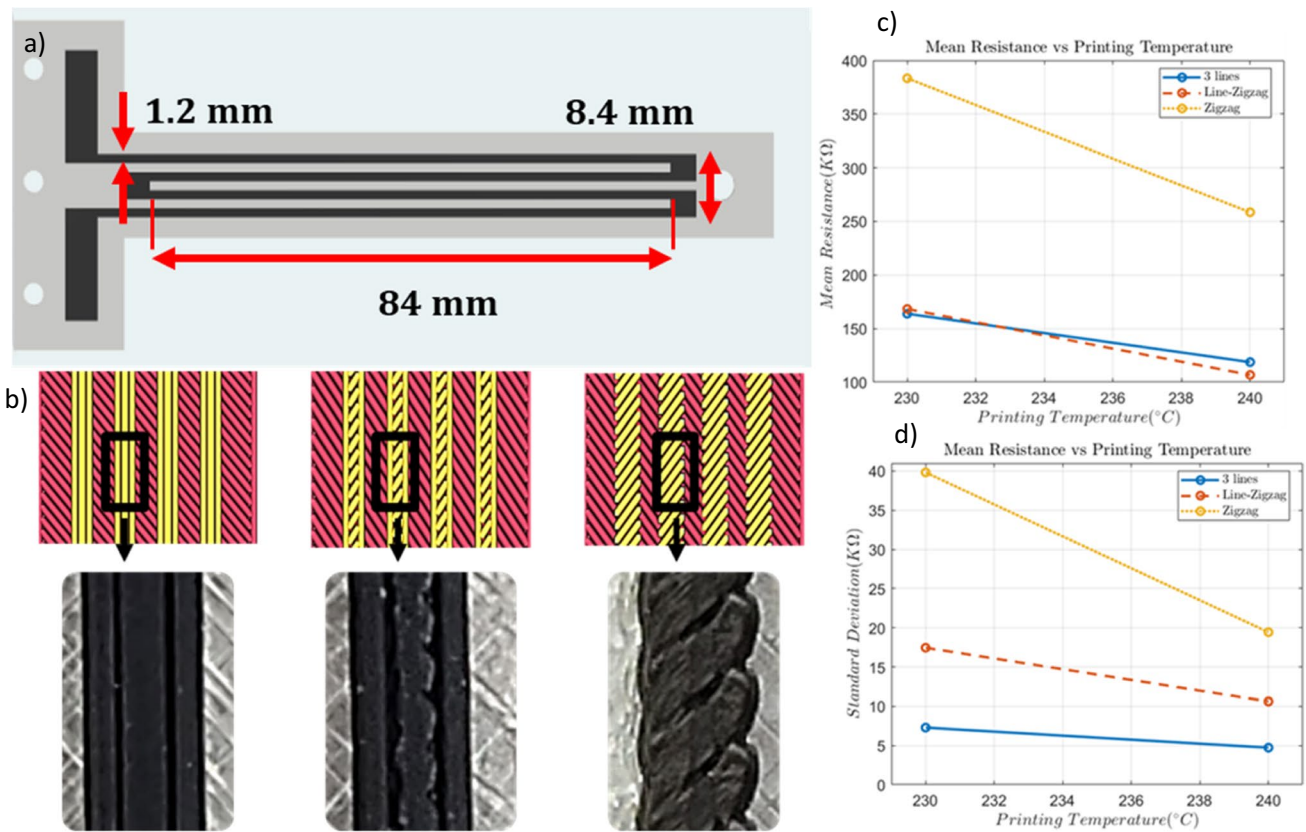


Fig. 5 (a) CAD model of the studied strain gauge, and (b) theoretical printing pattern in the slicing software (yellow = CPLA, red = TPU substrate) and actual 3D printed tracks (c) mean resistance vs printing temperature, and (d) standard deviation vs printing temperature

mean electrical resistance and also the standard deviation (a total of 3 repetitions for each pattern) decreases (see Fig. 5c d). For a good understanding of the percolation theory the authors suggest referring to [57]).

- At $T_p = 240^\circ C$, the best printing pattern in terms of minimized electrical resistance is B (line- zigzag- line) providing a mean resistance of 106,7 kΩ and a reduction of electrical resistance of 11.9% and 142% compared respectively to A (lines) and C (zigzag). This result can be portrayed in the following way: pattern B provides the best current path [58] compared to the other two possible patterns, resulting in low electrical resistance.
- The combination of the printing pattern and printing temperature that minimizes both electrical resistance and the standard deviation is “line-zigzag-line” and “240 °C”, which will be used for the embedded strain gauge fabricated into the finger.

3.2.2 Capacitive sensor

Over the tip of the finger, a capacitive sensor has been manufactured to obtain direct and real-time feedback (change in capacitance), when the tip of the finger touches objects.

The proposed capacitive sensor design is shown in Fig. 6a. It is made up of 4 main elements: a bottom electrode (0.6 mm thick), a separator layer (1 mm thick), a top electrode (0.6 mm thick) and a top plastic coverage (0.2 mm thick), for an overall thickness of 2.4 mm and the length and width are 21 mm and 14 mm.

The equation governing the proposed sensor is:

$$C = \frac{A}{d} \epsilon_0 \epsilon_s \tag{4}$$

where C is the capacitance of the sensor (nF), A is the surface area of the electrodes (mm^2), d is the electrode distance (also known as separator layer thickness) (mm), ϵ_0 is the vacuum dielectric constant ($\frac{pF}{mm}$) and ϵ_d is the relative dielectric constant of the separator layer, in particular, the latter can be expressed as

$$\epsilon_s = \epsilon_{air} * \%V_{air} + \epsilon_e * \%V_e \tag{5}$$

where ϵ_{air} is the air relative dielectric constant, ϵ_e is the relative elastomeric dielectric constant ($\frac{pF}{mm}$) while $\%V_{air}$ and $\%V_e$ are respectively the percentage of volume of

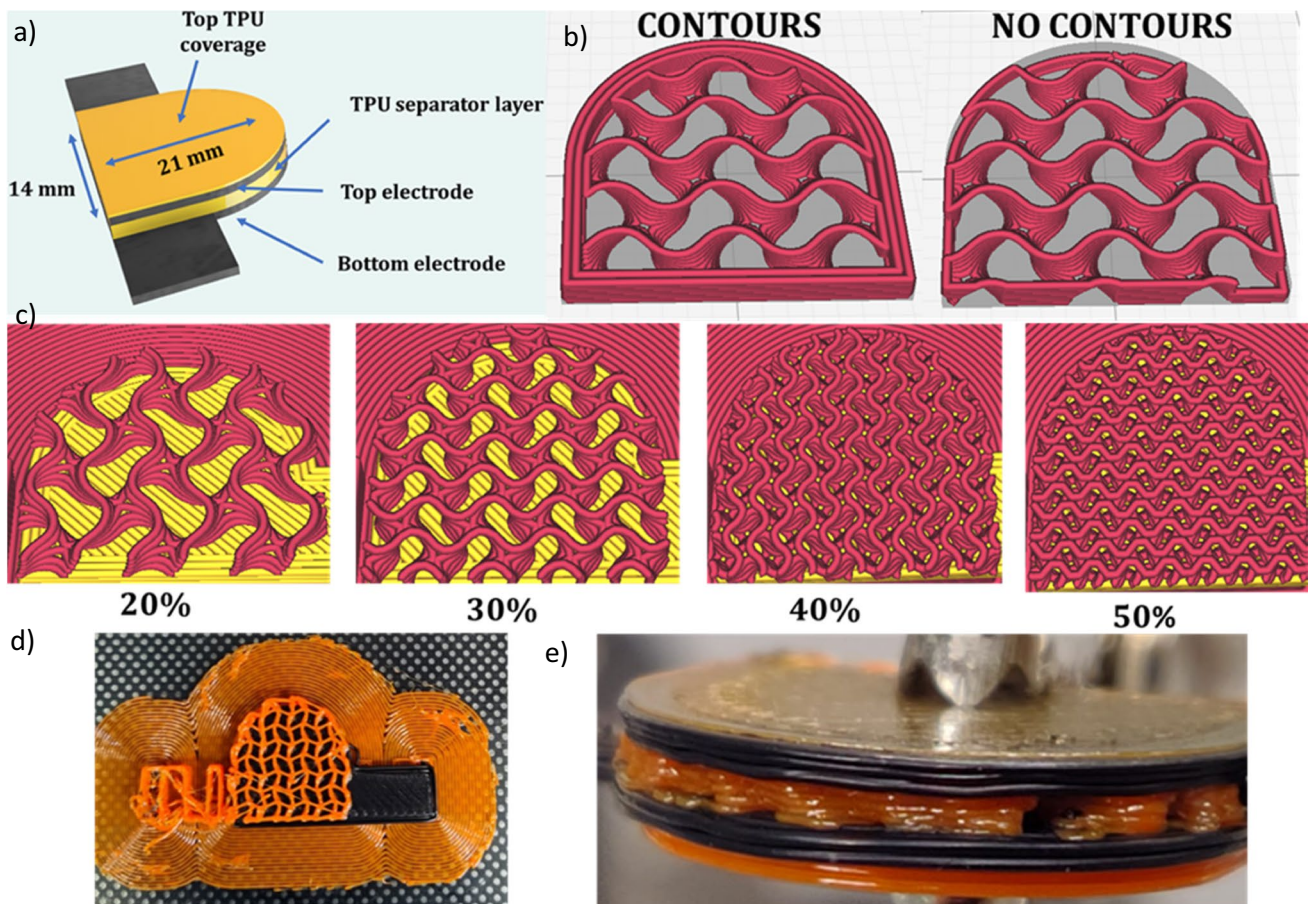


Fig. 6 (a) Capacitive sensor (b) contours vs no contours, (c) different infill percentage, (d) capacitive sensor during the manufacturing process, and (e) magnification of the manufactured sensor, it is possible to appreciate the air gaps into the separator layer

air and elastomeric material (it is important to point out that $\epsilon_{air} = 1$ and that $\epsilon_e > \epsilon_{air}$).

As well-known from scientific literature [59, 60], the separator layer needs to be a porous-based structure with air gaps due to the following reasons:

- When a force is applied, it shows more flexibility (with the same applied force, the distance among the electrodes will be greatly reduced in the case of a separator layer with air voids compared to a full separator structure) resulting in a greater capacitance change
- The percentage of the volume of air gaps ($\%V_{air}$) will be reduced under a force/pressure stimulus whereas the percentage of the volume of the elastomeric material ($\%V_e$) will increase resulting in a greater capacitance change ($\epsilon_e > \epsilon_{air}$).

The separator layer has been designed (Fusion 360, Autodesk) as a full structure: the porous structure (air gaps) has been generated into the slicing software (Ultimaker Cura 4.11.0) using gyroid infill (well known in the

scientific literature for providing a good response when it is compressed [61]).

It is important to point out that the separator layer needs to be fabricated without any contour, otherwise the structure would be more rigid, and a huge amount of force will be required to compress the solid contours resulting in less sensor sensitivity (see Fig. 6b). To achieve this goal, three process parameters have been successfully set: wall line count, top layer, and bottom layer, respectively as 0, 0 and 0.

For the fabrication of the separator layer the TPU 85 A NinjaFlex (henceforth TPU), (NinjaTek, USA), was used due to the need to produce a separator layer as flexible as possible, to obtain a good sensor sensitivity.

Further details about process parameters are listed in Supplementary information (Table S3). As shown in Fig. 6c four different infill percentages of the gyroid separator layer were studied: 20%, 30%, 40% and 50%.

Two different conductive materials were used, CTPU and CPLA (material data are available in Table S4), to study the best one in terms of sensor sensitivity.

After printing the capacitive sensors with different infill percentages of the separator layer and conductive material for the electrodes, the following conclusions can be drawn-

- Using CPLA and printing the separator layer setting 20% infill, 8 prints on 10 have failed, showing manufacturing inconsistency: the separator layer act as “support structure” during the manufacturing process and being not dense enough the top electrode collapse when printed. The top electrode meets the bottom one: no capacitance values can be read (instead resistance values were read).
- Using CPLA and increasing the separator layer percentage (30%, 40% and 50%) the previous issue has been solved.
- Using CTPU, it was possible to print the separator layer setting 20% infill (10 prints on 10) unlike for the CPLA. The authors justify the following behavior as follows: being CTPU made of TPU (82% TPU and 18% carbon black) the adhesion between the previous substrate (TPU) and the first electrode layer is abruptly increased if compared to CPLA.
- Increasing the infill percentage (from 20 to 50%) for both conductive materials, the capacitance value of the final sensor (after wiring, at rest) increases too because the percentage of TPU volume increases while the percentage of air volume decreases.

After connecting electrical wires to the pads, the sensors have been characterized. The measurement protocol used is the following: calibrated weights have been placed over the capacitive sensor and the capacitance value has been recorded using a digital multimeter.

In particular, the applied weight has been increased in the following way: 0, 200, 400, 800, 1000, 1500, 2000, 2500, 3000, 3500 g. A force sensor has been placed under the proposed capacitance sensor to record actual applied force values.

Results are shown in Fig. 7a and b.

From the characterization of the capacitive sensors, it stands out:

- Increasing the infill percentage, the performance (sensitivity) of the capacitive sensor decreases both for CTPU and CPLA.
- At the same infill percentage (30, 40 and 50%) the behavior of the CPLA and CTPU sensors is the same showing that the only reason to choose CTPU instead of CPLA is because of its composition allowing it to be 3D printed setting the separator layer at 20% infill.
- Every curve has in common an initial straight line in which the capacitance changes with a small amount of force and a second phase characterized by a sort of saturation in which a huge force is required to slightly change the capacitance (i.e., in 20% CTPU to achieve a 23% in $\Delta C/C_0$ almost 10 N are required while to switch from 23 to 25% (2% increase) almost 15 N are required).
- CTPU 20% infill is the best sensors in terms of sensitivity, calculated as the ratio of incremental output to incremental input.

$$S = \frac{\Delta C}{\Delta F} \tag{6}$$

And it has been calculated in the linear region of the curve (from 0 N to 16,6 N corresponding to 0 g to 1000 g applied on the sensor) and is: $S = 0.53 \frac{\mu F}{N}$, with a minimum detectable change of capacitance force of 1.9 N.

- Also, 20% infill is the best solution not only for the higher sensitivity but also because the amount of material used during the fabrication is reduced (and the time too).

One more test has been performed to evaluate the stability of the best sensor (see Fig. 7c): a 200 g weight (which corresponds to the minimum force detectable from the sensor) was applied for 2 s, removed for 2 s, and applied again for

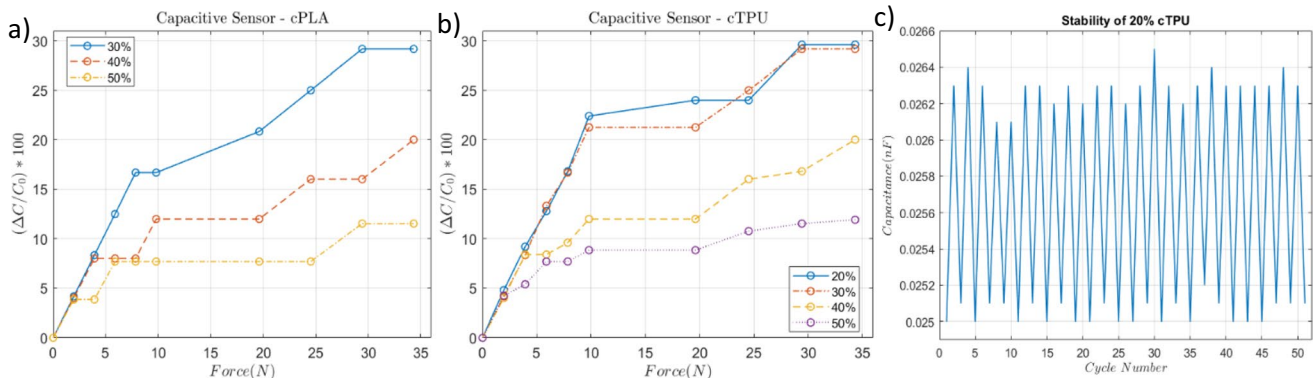


Fig. 7 Capacitive sensors results (a) CPLA sensitivity at different infill percentage of the separator layer, (b) CTPU sensitivity at different infill percentage of the separator layer, and (c) CTPU stability at 20% of infill percentage when 50 consecutive force cycles are applied

the same amount of time, for a total of 50 cycles. The sensor shows high stability, and it can be used as an ON/OFF sensor to detect a minimum applied weight of 200 g (force of 1.9 N).

In conclusion, although the sensitivity of the sensor is almost 2/3 order of magnitude less than the ones fabricated using traditional approaches, it can be used as ON/OFF sensors: the following advantages have been achieved using this manufacturing method-

- Only one fabrication method is involved (in the traditional approach at least 3)
- 0 assembly tasks are required (in the traditional approach at least 3)
- It is possible to create smart structures embedding the following sensor in the same printing cycle.

4 Additive manufacturing and characterization

4.1 Additive manufacturing

For the manufacturing of the proposed finger with the two embedded sensors and the integration of the SMA spring, a commercial low-cost (350 \$) dual extruder machine based on the IDEX (independent dual extrusion) mechanism was used (Tenlog TL D3 Pro, Tenlog 3D Solutions, USA). Three different filaments were extruded from 2 nozzles: PCL (for the finger, nozzle 1), CTPU (for both the sensor's active parts, nozzle 2) and TPU (for the separator layer and top coverage of the capacitive sensor, nozzle 1).

Several G-code modifications have been made (see supplementary file S6) due to the following reasons: (i) to print at 70 °C, (ii) to stop the print at a certain layer number to embed the SMA spring and (iii) to stop the print at a selected layer height to change the filament (from PCL to TPU) to print the separator layer and the top cover of the capacitive sensor.

The filament change procedure used in the present work consists on (i) stopping the printing process (thanks to the G-code modification), (ii) manually changing the material (from PCL to TPU) by following the 3D printer changing filament procedure, (iii) extruding 10 m of the new filament in the build-plate corner in order to clean the nozzle from the previous filament, and (iv) resuming the print.

The most important process parameters used are summarized in Table 4: two 0.4 mm nozzles were employed, and 0.2 mm was set as layer height parameter (same value for each material).

In the slicing software, the 3D Printer was instructed to pause immediately following a critical layer (see Supplementary information): this layer represented half of the diameter

of the holes in which the SMA nickel-titanium spring will be placed. Along with this instruction, the 3D Printer was also made to maneuver its axes to present the partial-completed print to the Cartesian Pick and Place Robot (CPPR): a custom-made machine developed as a small-form-factor alternative to larger, more industrial, and expensive versions. As it is composed of a 400 × 330 mm aluminum framework and 3D printed components, the design is highly modifiable and easily integrated with other machines. It is controlled with an Arduino Uno, as well as three A4988 Bipolar Stepper Motor Drivers, and utilizes a custom-written G-Code interpreter. The CPPR (see Fig. 8a) has been able to use two electromagnets to manipulate the steel crimped SMA actuators into the desired position. These electromagnets are simultaneously activated through an Omron relay module, which is controlled by the Arduino using G-Code over a serial connection to the host computer. This method enabled precise delivery of the SMA actuators without direct action from the user. More details about the custom-made CPPR are provided in Supplementary materials S7.

After placing the SMA spring, the print was resumed and the PCL filament was extruded above to spring to completely embed it into the finger: as discussed before, it is crucial that the temperature of the extruded filament above the SMA is lower than A_s to avoid SMA activation. The PCL temperature above the SMA was measured by means of infrared thermal imaging: as shown in Fig. 8b, as soon as the filament flows out from the nozzle, due to the interaction with the air its temperature abruptly decreases from 70 °C (printing temperature) to 36.6 °C: the temperature of the just extruded PCL bead over the SMA is 36.6 °C, ensuring the

Table 4 Process parameters used for the finger for the finger fabrication

Parameter	PCL	CTPU	TPU
Printing temperature (°C)	70	240	225
Line width (mm)	0.4	0.4	0.4
Printing speed ($\frac{mm}{s}$)	• 15	20	25
	• 10 (near the corner)		
Flow (%)	110	120	107
Retraction (mm)	4	2.5	6
Infill percentage (%)	20	100	• 20% (separator layer) • 100 (top coverage)
Infill pattern	lines	• Line-zigzag-line (strain gauge) • Line (capacitive electrodes)	lines

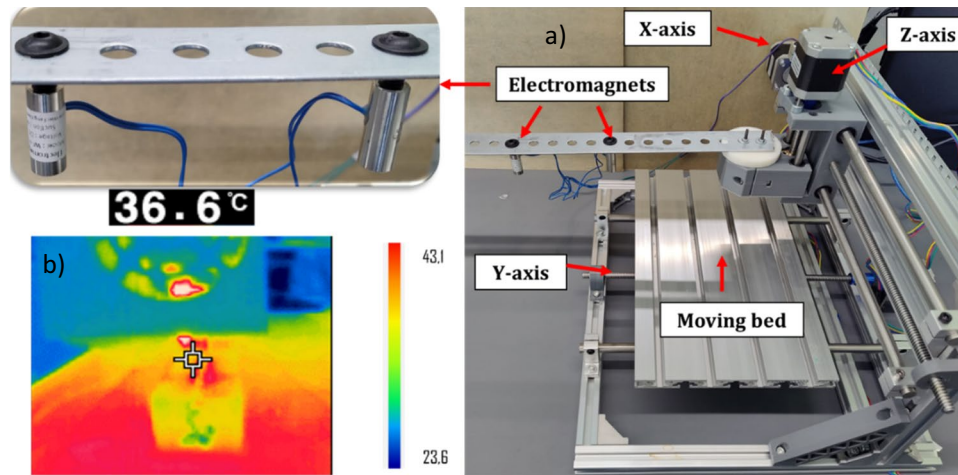


Fig. 8 (a) Custom-made Cartesian pick and place robot (CPPR) for SMA spring placement. (b) Infrared image during the 3D printing process: the central marker (temperature of 36.6 °C) refers to the just extruded PCL filament over the embedded SMA spring, proving that

the temperature of the filament in contact with the SMA is less than its austenitic start temperature. Moreover, the highest temperature is reached on the build plate (43.1 °C) to guarantee a good adhesion between the plate and the extruded PCL layers

preservation of the SMA martensite structure and avoiding any SMA activation.

In Fig. 9, the manufacturing steps and the final finger are shown.

The total cost of the proposed finger, computed by the slicing software as a function of the amount of material employed during the manufacturing process, is 1.2 \$, while the total printing time was 2 h and 51 min, which needs to be increased of almost 10 min to embed the SMA using the CPPR and to change material (from PCL to TPU).

In Table 5, a summary of the benefits brought from the proposed manufacturing approach over a traditional manufacturing approach are listed.

4.2 Characterization

The proposed finger has been characterized with several tests to evaluate: (i) PCL material behavior in terms of hysteresis, (ii) bending angle of the finger and its motion, (iii) correlation among change in resistance (embedded strain gauge) and bending angle, and (iv) usage of the capacitive sensor as ON/OFF sensor when the finger touches objects.

For the characterization test, a custom-made setup shown in Fig. 10a was used.

It consists of the following elements:

- i) A custom-made bracket where the terminal block of the finger has been attached used screws, nuts, and bolts.
- ii) A digital camera (Canon EOS 70D) to take video, to calculate bending angle and joint position in the 2D space.
- iii) Two digital multimeters, to take measurements of resistance and capacitance.

iv) A power supply (BK Precision 9116) to provide current input to the SMA in accordance with the desired frequency.

v) A custom-made circuit to calculate the voltage when current is provided to the SMA.

The following protocol was employed to characterize the finger: a current input of 3.2 A (chosen in accordance with the previous SMA characterization, Sect. 2.2) was applied to the SMA for 2 s followed by a cooling time of 50 s (in that period a dead weight of 100 g was applied to the finger to get it back at its rest position) for a total of 10 cycles.

Furthermore, two fingers were characterized: the one described so far (SMA spring completely embedded) and one more fabricated by embedding the SMA spring only into the two end parts (SMA partially embedded) shown in Fig. 10b, to understand the best SMA spring position.

5 Results and discussion

The bending angle and the position into the 2D space of each phalanx were measured as shown in Fig. 10c. The results in terms of bending angle are shown in Fig. 10d for both versions of the finger: “SMA completely embedded” and “SMA partially embedded”, as well as the finger tracking into 2D space for the “SMA completely embedded” (Fig. 10e).

The following considerations can be pointed out:

- For both configurations, the initial cycles (only cycle one for “SMA completely embedded” and cycle one

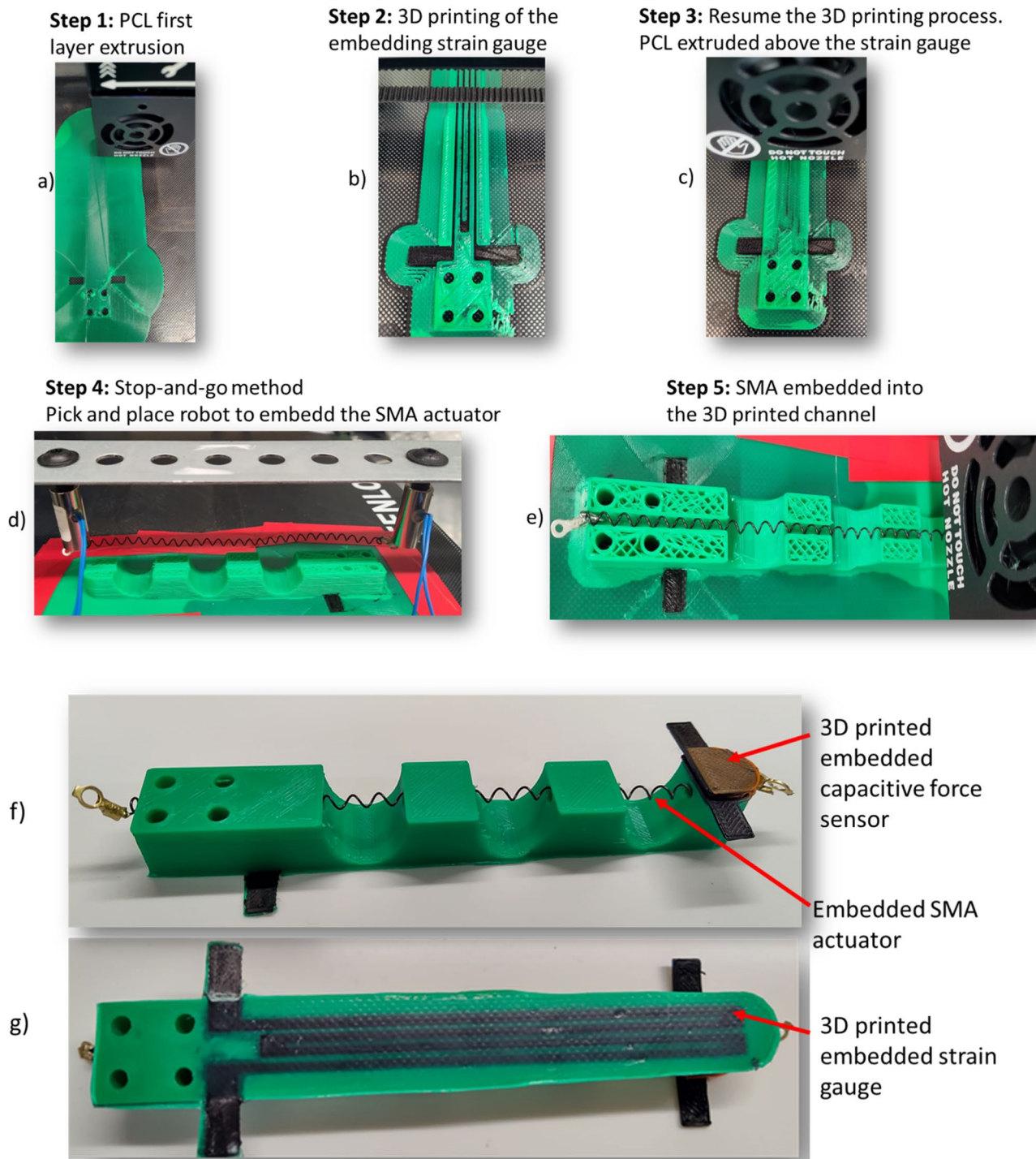


Fig. 9 Proposed manufacturing process to create a soft PCL finger with embedded sensors and SMA spring actuator: (a) first step: 3D printed PCL layer, (b) second step: 3D printed strain gauge, (c) third step: PCL coverage above the strain gauge, (d) fourth step: stop of the

printing process and usage of the CPPR robot to embed the SMA into the channel, (e) SMA into the channel, (f) manufactured finger top view, and (g) manufactured finger bottom view

and two for its counterpart) are characterized by a smaller bending angle, subsequently the bending angle increases becoming constant in a certain range:

for the “SMA completely embedded” the mean bending angle from cycle 2 to cycle 10 is 37.3° with a standard deviation of 0.13° , for its counterpart the mean bending

Table 5 Main difference between the proposed manufacturing approach and a traditional approach, considering the fabrication of a structure equipped with 2 sensors and 1 actuator

	Proposed approach	Traditional approach
Number of manufacturing steps	1	3 (soft finger, piezoresistive sensor, capacitive sensor)
Number of manual assembly tasks	0	3 (2 assembly tasks for the sensors and 1 assembly task for the SMA)
Manufacturing time	2 h 51 min	Unknown (manual assembly time to take into account)
Setup time	<ul style="list-style-type: none"> • 10 min (material change) • 20 min (calibration of CPPR machine for SMA embedding) • Time for the G-code modification (highly related to the engineer’s knowledge: we estimated 20 min) 	Unknown
Automation degree	Improved	Medium

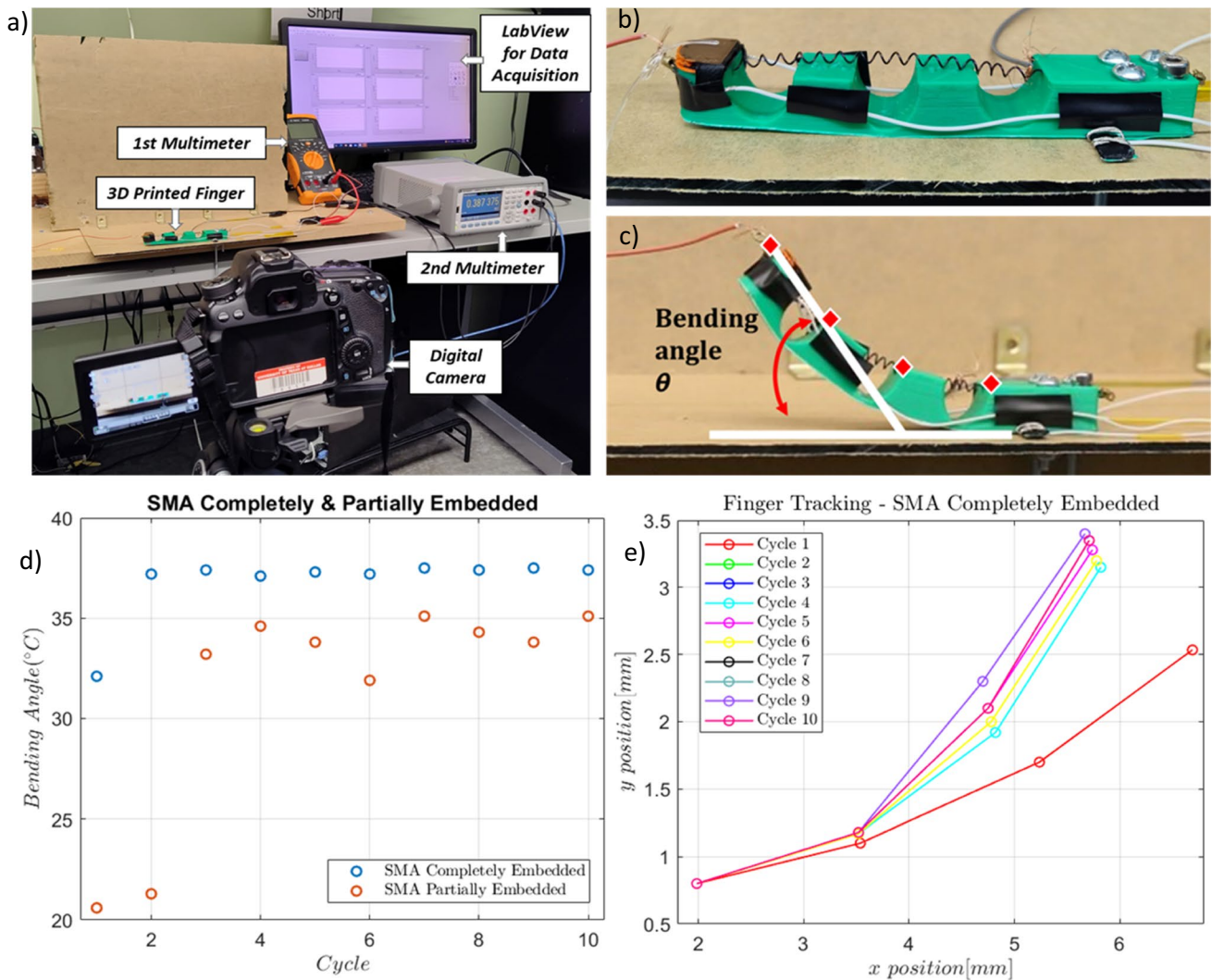


Fig. 10 (a) Characterization setup (b) Finger with partially embedded SMA spring (embedded only into the two end parts) (c) Bending angle and phalanx position in 2D space (d) bending angle for both

fingers version, (e) finger tracking in 2D space for the finger with embedded SMA (several x- and y- position from cycle 2 to cycle 10 overlap each other)

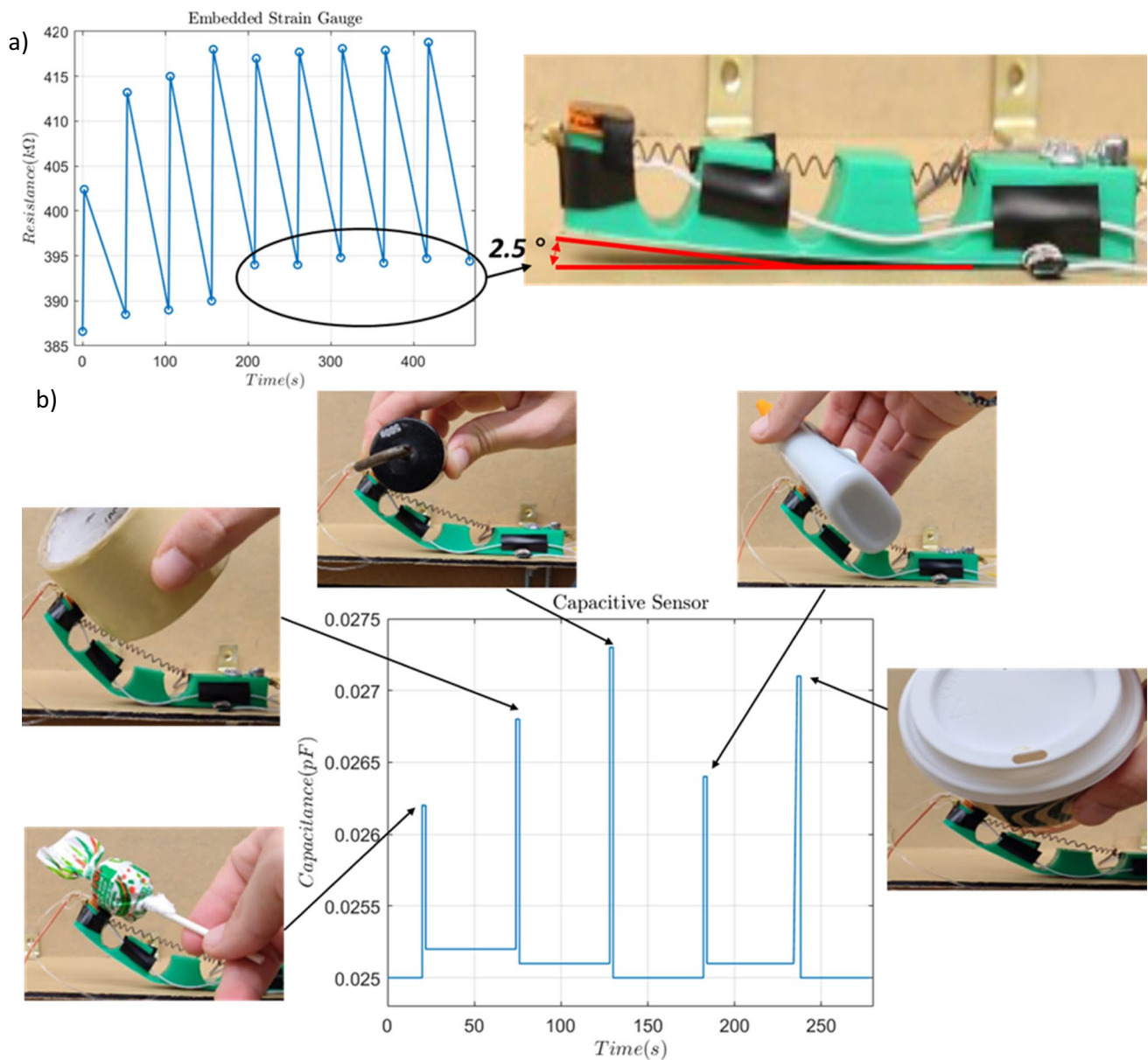


Fig. 11 (a) Strain gauge characterization. (b) Capacitive sensor embedded into the finger

angle from cycle 3 to cycle 10 is 33.9° with a standard deviation of 0.99° . The change in the bending angle from the first cycles to the last ones can be addressed to the Mullins effect, affecting thermoplastic materials.

- The “SMA completely embedded” version is better than its counterpart not only because the mean bending angle is 9.1% higher but also because the standard deviation is less.
- From the finger tracking diagram, it stands out that the finger movement (the movement of each phalange) mimics very well the human finger motion, proving how the Mutlu et al. [24] design rules are important to achieve this goal.

The change in bending angle has been correlated to the change of resistance provided by the embedded strain gauge (see Fig. 11a): the measured data were fitted, obtaining the following linear regression equation:

$$y = 0.6748x + 390.79 \quad (7)$$

With $R^2 = 0.93$.

From Eq. (7), the sensitivity of the strain gauge is found to be $674.8 \frac{\Omega}{^\circ}$.

Figure 11a shows that for the first cycle the change in resistance is less, in accordance with a smaller bending angle, while from cycle 2 to cycle 10 the change in

resistance is almost constant. Moreover, from cycle 5 up to cycle 10 the resting point is slightly higher than the one obtained for the previously cycles: this behavior is attributable to the PCL hysteresis, as a matter of fact from cycle 5 the finger does not get back in its original rest position (the bending angle between the bottom part of the finger and the support is 2.5° instead of 0°).

The capacitive sensor (already characterized in Section 3.2.2) having a sensitivity of $0.53 \frac{\mu F}{N}$, has been used in conjunction with different objects (adhesive tape, calibrated weight, lollipop, glue, and coffee cup) placed randomly into the 3D space, mimicking a real scenario. As shown in Fig. 11b the capacitive sensor provides fast feedback as soon as it gets into contact with target objects, getting back to its initial capacitance value when the finger is no longer pushing against the object. The following result suggests that this kind of sensor can be used at least as ON/OFF sensor to provide direct feedback about the presence/absence of objects: to achieve this aim, more characterization steps are required (for example a deep study about the interaction among the material surface of the object and the capacitive sensor). As shown in [62], the benefits due to the exploitation of force sensors over the soft finger tip are many and can potentially make these devices really appealing for the biomedical field.

It is worth mentioning that the following limitations have been found in the present study:

- The modification of the G-code requires experience in the 3D printing field: the following manufacturing approach cannot be used from makers and hobbyists. In particular, the integration of another system (pick and place robot) requires further studies to create a unique software able to communicate at the same time with the 3D printing and the pick and place robot.
- The strain gauge hysteresis needs to be compensated to obtain feedbacks useful for real-life applications
- Although the SMA activation is really fast (about 2 s) compared to other actuation systems such as shape memory polymers, the cooling time is still quite high (about 10 s) and future studies are required to reduce it.
- The proposed finger can be immediately activated after the removal from the 3D printing machine, providing real-time feedback thanks to the two 3D printed embedded sensors.
- A new manufacturing approach to embed actuators (SMA springs) into 3D printed structures has been presented. The main pillars of the proposed approach are: (i) the usage of PCL material because its printing temperature is less than the austenitic start temperature of the embedded SMA, (ii) the exploitation of the stop and go method to embed the SMA actuator and, (iii) the usage of a custom-made cartesian pick and place robot to reduce manual tasks and increases the placement accuracy.
- Two process parameters were studied to reduce the strain gauge electrical resistance, which has been reduced by 142% compared to the worst parameters set, to reduce power losses during its usage.
- Several tests were carried out to characterize each element of the proposed finger: (i) the best current input for the activation of the SMA was found to be 3.2 A, (ii) the capacitive sensor sensitivity was found to be $0.53 \frac{\mu F}{N}$ and (iii) the strain gauge sensitivity that was used to detect the finger bending angle, was $674.8 \frac{\Omega}{^\circ}$.

The proposed fabrication method paves the way for huge exploitation of the inexpensive FFF technology for the embedding of SMA, or other kinds of thermally activated actuators, like twisted coiled polymers (TCP), into complex FFF structures reducing human tasks and increasing placement accuracy. Future studies will be focused on the developing of a standardize fabrication method, based on the proposed approach, that can be used for the fabrication of several objects with embedded sensors and actuators. Moreover, several soft robots and gripper systems can be manufactured by embedding both sensing elements and actuators, resulting in assembly-free structures.

Supplementary Information The online version contains supplementary material available at <https://doi.org/10.1007/s00170-022-10556-x>.

Author contribution GS, SMAIO, JER: formal analysis, investigation, methodologies, writing- original draft.

MC, GP, YT: Project Administration, Supervision, Writing- review and editing, Resources.

Funding Open access funding provided by Politecnico di Bari within the CRUI-CARE Agreement.

Declarations

Ethics approval Ethical approval is not applicable in this study.

Competing interest The authors declare no competing interests.

Open Access This article is licensed under a Creative Commons Attribution 4.0 International License, which permits use, sharing,

6 Conclusions

The main findings of the present papers can be summarized as follows:

- A soft robotic finger composed of two embedded sensors (piezoresistive and capacitive sensor) has been 3D printed in a single cycle recurring to Material Extrusion (MEX) technology. The proposed finger was equipped with an embedded external shape memory alloy (SMA) actuator.

adaptation, distribution and reproduction in any medium or format, as long as you give appropriate credit to the original author(s) and the source, provide a link to the Creative Commons licence, and indicate if changes were made. The images or other third party material in this article are included in the article's Creative Commons licence, unless indicated otherwise in a credit line to the material. If material is not included in the article's Creative Commons licence and your intended use is not permitted by statutory regulation or exceeds the permitted use, you will need to obtain permission directly from the copyright holder. To view a copy of this licence, visit <http://creativecommons.org/licenses/by/4.0/>.

References

- Sheydaei E, Ibadode OO, Hu E, Pilliar R, Kandel R, Toyserkani E (2021) Additive manufacture of porous ceramic proximal interphalangeal (PIP) joint implant: design and process optimization. *Int J Adv Manuf Technol* 115(9–10):2825–2837. <https://doi.org/10.1007/s00170-021-07283-0>
- Stano G, Percoco G (2021) Additive manufacturing aimed to soft robots fabrication : a review. *Extrem Mech Lett* 42:101079. <https://doi.org/10.1016/j.eml.2020.101079>
- Schmitt F, Piccin O, Barbé L, Bayle B (2018) Soft robots manufacturing: a review. *Front Robot AI* 5:84. <https://doi.org/10.3389/frobt.2018.00084>
- Gul JZ et al (2018) 3D printing for soft robotics—a review. *Sci Technol Adv Mater* 19(1):243–262. <https://doi.org/10.1080/14686996.2018.1431862>
- Wallin TJ, Pikul J, Shepherd RF (2018) 3D printing of soft robotic systems. *Nat Rev Mater* 3(6):84–100. <https://doi.org/10.1038/s41578-018-0002-2>
- Yap YL, Sing SL, Yeong WY (2020) A review of 3D printing processes and materials for soft robotics. *Rapid Prototyp J* 26(8):1345–1361. <https://doi.org/10.1108/RPJ-11-2019-0302>
- Shintake J, Cacucciolo V, Floreano D, Shea H (2018) Soft robotic grippers. *Adv Mater* 30(29):1707035. <https://doi.org/10.1002/adma.201707035>
- Zolfagharian A, Mahmud MAP, Gharai S, Bodaghi M, Kouzani AZ, Kaynak A (2020) 3D/4D-printed bending-type soft pneumatic actuators: fabrication, modelling, and control. *Virtual Phys Prototyp* 15(4):373–402. <https://doi.org/10.1080/17452759.2020.1795209>
- Georgopoulou A, Egloff L, Vanderborght B, Clemens F (2021) A sensorized soft pneumatic actuator fabricated with extrusion-based additive manufacturing. *Actuators* 10(5):102. <https://doi.org/10.3390/act10050102>
- Elgeneidy K, Neumann G, Jackson M, Lohse N (2018) Directly printable flexible strain sensors for bending and contact feedback of soft actuators. *Front Robot AI* 5:1–14. <https://doi.org/10.3389/frobt.2018.00002>
- Yang Y, Chen Y (2017) Innovative design of embedded pressure and position sensors for soft actuators. *IEEE Robot Autom Lett* 3(2):656–663
- Stano G, Arleo L, Percoco G (2020) Additive manufacturing for soft robotics: design and fabrication of airtight, monolithic bending PneuNets with embedded air connectors. *Micromachines* 11(5):485. <https://doi.org/10.3390/mi11050485>
- Ragolia MA, Lanzolla AM, Percoco G, Stano G, Di Nisio A (2021) Thermal characterization of new 3d-printed bendable, coplanar capacitive sensors. *Sensors* 21(19):6324. <https://doi.org/10.3390/s21196324>
- Valvez S, Reis PNB, Susmel L, Berto F (2021) Fused filament fabrication-4d-printed shape memory polymers: a review. *Polymers (Basel)* 13(5):1–25. <https://doi.org/10.3390/polym13050701>
- Ehrmann G, Ehrmann A (2021) 3D printing of shape memory polymers. *J Appl Polym Sci* 138(34):1–11. <https://doi.org/10.1002/app.50847>
- Huang X, Panahi-Sarmad M, Dong K, Li R, Chen T, Xiao X (2021) Tracing evolutions in electro-activated shape memory polymer composites with 4D printing strategies: a systematic review. *Compos Part A Appl Sci Manuf.* 147:106444. <https://doi.org/10.1016/j.compositesa.2021.106444>
- Garces IT, Ayranci C (2021) Advances in additive manufacturing of shape memory polymer composites. *Rapid Prototyp J* 27(2):379–398. <https://doi.org/10.1108/RPJ-07-2020-0174>
- Nam S, Pei E (2020) The influence of shape changing behaviors from 4D printing through material extrusion print patterns and infill densities. *Materials (Basel)* 13:17. <https://doi.org/10.3390/MA13173754>
- Wang W, Ahn SH (2017) Shape memory alloy-based soft gripper with variable stiffness for compliant and effective grasping. *Soft Robot* 4(4):379–389. <https://doi.org/10.1089/soro.2016.0081>
- Mao Y, Yu K, Isakov MS, Wu J, Dunn ML, Jerry Qi H (2015) Sequential self-folding structures by 3D printed digital shape memory polymers. *Sci Rep* 5:1–12. <https://doi.org/10.1038/srep13616>
- Ge Q, Dunn CK, Qi HJ, Dunn ML (2014) Active origami by 4D printing. *Smart Mater Struct* 23(9):094007. <https://doi.org/10.1088/0964-1726/23/9/094007>
- Al-Rubaia M, Pinto T, Qian C, Tan X (2019) Soft actuators with stiffness and shape modulation using 3D-printed conductive polylactic acid material. *Soft Robot* 6(3):318–332. <https://doi.org/10.1089/soro.2018.0056>
- Yamamura S, Iwase E (2021) Hybrid hinge structure with elastic hinge on self-folding of 4D printing using a fused deposition modeling 3D printer. *Mater Des* 203:109605. <https://doi.org/10.1016/j.matdes.2021.109605>
- Mutlu R, Alici G, In het Panhuis M and Spinks GM (2016) 3D printed flexure hinges for soft monolithic prosthetic fingers. *Soft Robot* 3 (3):120–133. <https://doi.org/10.1089/soro.2016.0026>
- Mohammadi A et al (2020) A practical 3D-printed soft robotic prosthetic hand with multi-articulating capabilities. *PLoS ONE* 15(5):1–23. <https://doi.org/10.1371/journal.pone.0232766>
- Rodrigue H, Wang W, Kim DR, Ahn SH (2017) Curved shape memory alloy-based soft actuators and application to soft gripper. *Compos Struct* 176:398–406. <https://doi.org/10.1016/j.composit.2017.05.056>
- Rodrigue H, Wang W, Bhandari B, Han MW, Ahn SH (2015) SMA-based smart soft composite structure capable of multiple modes of actuation. *Compos Part B Eng* 82:152–158. <https://doi.org/10.1016/j.compositesb.2015.08.020>
- Lee JH, Chung YS, Rodrigue H (2019) Long shape memory alloy tendon-based soft robotic actuators and implementation as a soft gripper. *Sci Rep* 9(1):11251. <https://doi.org/10.1038/s41598-019-47794-1>
- Rodrigue H, Bhandari B, Han MW, Ahn SH (2015) A shape memory alloy-based soft morphing actuator capable of pure twisting motion. *J Intell Mater Syst Struct* 26(9):1071–1078. <https://doi.org/10.1177/1045389X14536008>
- Akbari S, Sakhaei AH, Panjwani S, Kowsari K, Ge Q (2021) Shape memory alloy based 3D printed composite actuators with variable stiffness and large reversible deformation. *Sensors Actuators A Phys* 321:112598. <https://doi.org/10.1016/j.sna.2021.112598>
- Akbari S, Sakhaei AH, Panjwani S, Kowsari K, Serjourei A, Ge Q (2019) Multimaterial 3D printed soft actuators powered by shape memory alloy wires. *Sensors Actuators, A Phys* 290:177–189. <https://doi.org/10.1016/j.sna.2019.03.015>
- Kabir SMF, Mathur K, Seyam AFM (2020) A critical review on 3D printed continuous fiber-reinforced composites: history, mechanism,

- materials and properties. *Compos Struct* 232:111476. <https://doi.org/10.1016/j.compstruct.2019.111476>
33. Díaz-Rodríguez JG, Pertúz-Comas AD, González-Estrada OA (2020) Mechanical properties for long fibre reinforced fused deposition manufactured composites. *Compos Part B Eng* 211(October):2021. <https://doi.org/10.1016/j.compositesb.2021.108657>
 34. Zhuo P, Li S, Ashcroft IA, Jones AI (2021) Material extrusion additive manufacturing of continuous fibre reinforced polymer matrix composites: a review and outlook. *Compos. Part B Eng.* 224:109143. <https://doi.org/10.1016/j.compositesb.2021.109143>
 35. Kim C, Sullivan C, Hillstrom A, Wicker R (2021) Intermittent embedding of wire into 3D prints for wireless power transfer. *Int J Precis Eng Manuf* 22(5):919–931. <https://doi.org/10.1007/s12541-021-00508-y>
 36. Arh M, Slavič J, Boltežar M (2020) Experimental identification of the dynamic piezoresistivity of fused-filament-fabricated structures. *Addit Manuf* 36:101493. <https://doi.org/10.1016/j.addma.2020.101493>
 37. Kim K, Park J, Hoon Suh J, Kim M, Jeong Y, Park I (2017) 3D printing of multiaxial force sensors using carbon nanotube (CNT)/thermoplastic polyurethane (TPU) filaments. *Sensors Actuators A Phys* 263:493–500. <https://doi.org/10.1016/j.sna.2017.07.020>
 38. Maurizi M et al (2019) Dynamic measurements using FDM 3D-printed embedded strain sensors. *Sensors (Switzerland)* 19(12):1–15. <https://doi.org/10.3390/s19122661>
 39. Loh LYW, Gupta U, Wang Y, Foo CC, Zhu J, Lu WF (2021) 3D Printed metamaterial capacitive sensing array for universal jamming gripper and human joint wearables. *Adv Eng Mater* 2001082:1–9. <https://doi.org/10.1002/adem.202001082>
 40. Alsharari M, Chen B, Shu W (2021) Sacrificial 3D printing of highly porous, soft pressure sensors. *Adv Electron Mater* 2100597:1–12. <https://doi.org/10.1002/aelm.202100597>
 41. Arh M, Slavič J (2022) Single-process 3D-printed triaxial accelerometer. *Adv Mater Technol* 7(7):2101321. <https://doi.org/10.1002/admt.202101321>
 42. Arh M, Slavič J, Boltežar M (2021) Design principles for a single-process 3d-printed accelerometer—theory and experiment. *Mech Syst Signal Process* 152:107475. <https://doi.org/10.1016/j.ymsp.2020.107475>
 43. Ceretti E, Ginestra P, Neto PI, Fiorentino A, Da Silva JVL (2017) Multi-layered scaffolds production via fused deposition modeling (FDM) using an open source 3D printer: process parameters optimization for dimensional accuracy and design reproducibility. *Procedia CIRP* 65:13–18. <https://doi.org/10.1016/j.procir.2017.04.042>
 44. Meng Z et al (2020) Design and additive manufacturing of flexible polycaprolactone scaffolds with highly-tunable mechanical properties for soft tissue engineering. *Mater Des* 189:108508. <https://doi.org/10.1016/j.matdes.2020.108508>
 45. Liu F et al (2018) Structural evolution of PCL during melt extrusion 3D printing. *Macromol Mater Eng* 303(2):1–6. <https://doi.org/10.1002/mame.201700494>
 46. Lee J, Walker J, Natarajan S, Yi S (2020) Prediction of geometric characteristics in polycaprolactone (PCL) scaffolds produced by extrusion-based additive manufacturing technique for tissue engineering. *Rapid Prototyp J* 26(2):238–248. <https://doi.org/10.1108/RPJ-08-2018-0219>
 47. Dey A, Yodo N (2019) A systematic survey of FDM process parameter optimization and their influence on part characteristics. *J Manuf Mater Process* 3(3):64. <https://doi.org/10.3390/jmmp3030064>
 48. Deng E, Tadesse Y (2021) A soft 3d-printed robotic hand actuated by coiled SMA. *Actuators* 10(1):1–24. <https://doi.org/10.3390/act101010006>
 49. Hamidi A, Almubarak Y, Tadesse Y (2019) Multidirectional 3D-printed functionally graded modular joint actuated by TCPFL muscles for soft robots. *Bio-Design Manuf* 2(4):256–268. <https://doi.org/10.1007/s42242-019-00055-6>
 50. Schouten M, Wolterink G, Dijkshoorn A, Kosmas D, Stramigioli S, Krijnen G (2021) A review of extrusion-based 3D printing for the fabrication of electro- and biomechanical sensors. *IEEE Sens J* 21(11):12900–12912. <https://doi.org/10.1109/JSEN.2020.3042436>
 51. Kwok SW et al (2017) Electrically conductive filament for 3D-printed circuits and sensors. *Appl Mater Today* 9:167–175. <https://doi.org/10.1016/j.apmt.2017.07.001>
 52. Daniel F, Patoary NH, Moore AL, Weiss L, Radadia AD (Nov.2018) Temperature-dependent electrical resistance of conductive polylactic acid filament for fused deposition modeling. *Int J Adv Manuf Technol* 99(5–8):1215–1224. <https://doi.org/10.1007/s00170-018-2490-z>
 53. Dijkshoorn A, Schouten M, Stramigioli S, Krijnen G (2021) Modelling of anisotropic electrical conduction in layered structures 3d-printed with fused deposition modelling. *Sensors* 21(11):1–37. <https://doi.org/10.3390/s21113710>
 54. Cardenas JA et al (2020) Flash ablation metallization of conductive thermoplastics. *Addit Manuf* 36:101409. <https://doi.org/10.1016/j.addma.2020.101409>
 55. Stano G, Di Nisio A, Lanzolla AM, Ragolia M, Percoco G (2020) Fused filament fabrication of commercial conductive filaments: experimental study on the process parameters aimed at the minimization, repeatability and thermal characterization of electrical resistance. *Int J Adv Manuf Technol* 111(9):2971–2986. <https://doi.org/10.1007/s00170-020-06318-2>
 56. Gupta SK, Talati M, Jha PK (2008) Shape and size dependent melting point temperature of nanoparticles. *Mater Sci Forum* 570:132–137. <https://doi.org/10.4028/www.scientific.net/MSF.570.132>
 57. MohdRadzuan NA, Sulong AB, Sahari J (2017) A review of electrical conductivity models for conductive polymer composite. *Int J Hydro Energ* 42(14):9262–9273. <https://doi.org/10.1016/j.ijhydene.2016.03.045>
 58. Tirado-Garcia I et al (2021) Conductive 3D printed PLA composites: on the interplay of mechanical, electrical and thermal behaviours. *Compos Struct* 265:113744. <https://doi.org/10.1016/j.compstruct.2021.113744>
 59. Li R et al (2021) “Research progress of flexible capacitive pressure sensor for sensitivity enhancement approaches”, *Sensors Actuators. A Phys* 321:112425. <https://doi.org/10.1016/j.sna.2020.112425>
 60. Atalay O, Atalay A, Gafford J, Walsh C (2018) A highly sensitive capacitive-based soft pressure sensor based on a conductive fabric and a microporous dielectric layer. *Adv Mater Technol* 3(1):1–8. <https://doi.org/10.1002/admt.201700237>
 61. Holmes DW et al (2021) Mechanical behaviour of flexible 3D printed gyroid structures as a tuneable replacement for soft padding foam. *Addit Manuf* 50:102555. <https://doi.org/10.1016/j.addma.2021.102555>
 62. Tripicchio P, D’Avella S, Avizzano CA, Di Pasquale F, Velha P (2020) On the integration of FBG sensing technology into robotic grippers. *Int J Adv Manuf Technol* 111(3–4):1173–1185. <https://doi.org/10.1007/s00170-020-06142-8>

Publisher's note Springer Nature remains neutral with regard to jurisdictional claims in published maps and institutional affiliations.